



# Structural, magnetic, and photocatalytic properties in $\text{Bi}_{0.83-x}\text{La}_{0.17}\text{Y}_x\text{FeO}_3$ nanoparticles

Razieh Sanavi Khoshnood<sup>1</sup> · Davoud Sanavi Khoshnoud<sup>2</sup>

Received: 10 April 2019 / Accepted: 25 September 2019 / Published online: 9 October 2019  
© Springer-Verlag GmbH Germany, part of Springer Nature 2019

## Abstract

In this research, polycrystalline  $\text{BiFeO}_3$  (BFO) and  $\text{Bi}_{0.83-x}\text{La}_{0.17}\text{Y}_x\text{FeO}_3$  nanoparticles ( $\text{BLY}_x\text{FO}$  NPs,  $x = 0.0, 0.05, 0.10, 0.15,$  and  $0.20$ ) were prepared by sol–gel route. The effect of  $\text{La}^{3+}$  and  $\text{Y}^{3+}$  co-doped ions on crystal structure, magnetic, and photocatalytic properties was reported. The Rietveld refinement of X-ray diffraction data confirms a consecutive structural phase transition of R3c–Pbam–pnma from BFO to  $\text{BLY}_{0.20}\text{FO}$  compound. The investigation of field-emission scanning electron microscopy (FE-SEM) images indicated that the morphology and distribution of nanoparticles are almost uniform. The energy-dispersive X-ray (EDAX) analysis confirms the elemental concentration in  $\text{BLY}_x\text{FO}$  NPs. All of  $\text{BLY}_x\text{FO}$  NPs revealed the weak ferromagnetic behavior. The highest magnetic parameters occur in the vicinity of the R3c/Pbam phase boundary in sample with  $x = 0$ . The change of magnetic behavior from BFO to  $\text{BLY}_0\text{FO}$  was discussed based on suppressing spiral cycloid spin structure and lattice distortion in rhombohedral phase. In compounds with orthorhombic structure, only lattice distortion can be affected magnetic behavior. The direct bandgap of all samples obtained from the UV–Vis diffuse reflectance spectra using Kabelka–Munk equation. The bandgap in  $\text{BLY}_x\text{FO}$  NPs decreases with substituting La ion and then increases with increasing Y content. The photocatalytic activity of BFO and  $\text{BLY}_x\text{FO}$  NPs is evaluated by the degradation of methyl orange in the presence of  $\text{H}_2\text{O}_2$  at pH value 2 under visible light. The photocatalytic properties enhance with doping La in BFO. However, the photocatalytic activity dependence on Y concentration has a behavior more complicated and is strongly depending on crystal structure.

## 1 Introduction

One of the interesting compounds based on perovskite structure with chemical formula  $\text{ABO}_3$  is  $\text{BiFeO}_3$  (BFO) compound. The BFO is a multiferroic material consists of simultaneous antiferromagnetism and ferroelectricity orders that from fundamental view point are very attractive [1, 2]. Besides this, due to high Curie ( $T_C = 830$  °C) and Neel ( $T_N = 370$  °C) temperatures of BFO, this compound is a good candidate for technological applications above room temperature [3]. The presence of the spiral spin structure and leakage current limited magnetic and electrical practical

applications in BFO, respectively [4, 5]. One of the methods for optimizing magnetic and electrical properties of BFO is doping various ions such as (La, Nd, Pr, Sm, Ho, Tb, ...) and (Ti, Cr, Co, Ni, Co, ...) at Bi and Fe sites, respectively [6–18]. One of the intriguing behaviors of BFO is the existence of numerous structural phases that depends on doping level of various ions for replacing Bi ion [8, 9]. Such occurrences create the morphotropic phase boundaries (MPB). For instance, it was shown that substituting  $\text{La}^{3+}$  ion with lower ionic radius compared to that of  $\text{Bi}^{3+}$  in  $\text{Bi}_{1-x}\text{La}_x\text{FeO}_3$ , first, the spiral cycloid spin structure (SCSS) in rhombohedral phase is suppressed, and then with increasing  $\text{La}^{3+}$  content, the SCSS is completely destroyed and polar rhombohedral structure is transformed into anti-polar structure with Pbam space group, and finally with more doping, structure is changed into new non-polar orthorhombic phase with Pnma space group and nonlinear G-type antiferromagnetism structure [10, 11]. The similar behavior was observed in  $\text{Bi}_{1-x}\text{RE}_x\text{FeO}_3$  ( $\text{RE} = \text{rare-earth ion}$  and  $\text{Y}^{3+}$ ) compounds in lower  $x$  value because of smaller ionic radius of rare earth ( $r_{\text{RE}}$ ) compared to  $r_{\text{Bi}} = 1.172$  Å and  $r_{\text{La}} = 1.17$

✉ Razieh Sanavi Khoshnood  
rskhoshnood@yahoo.com  
Davoud Sanavi Khoshnoud  
dskhoshnoud@semnan.ac.ir

<sup>1</sup> Department of Chemistry, Mashhad Branch, Islamic Azad University, Mashhad, Iran

<sup>2</sup> Faculty of Physics, Semnan University, P. O. Box 35195-363, Semnan, Iran

Å [12, 13]. Accordingly, various investigations have been also performed on La and RE co-doped BFO [19, 20].

In addition to interesting occurrences in structural, electrical, and magnetic properties of undoped and doped BFO, recently, various reports were carried out on the photocatalytic activity of BFO as a new candidate for removal of organic dye from water due to its small bandgap (2.0–2.5 eV) [21–24]. One of the challenges faced by photocatalytic degradation processes is to achieve high activity photocatalyst in visible light region for BFO. One of the best methods for improving photocatalytic properties of BFO is doping RE ions for Bi site [21–24].

There is another family of ferrite materials with hexagonal structure based on molar formula  $\text{BaFe}_{12}\text{O}_{19}$  (hexaferrite) that are also promising for practical application [25–27]. In substituted M-type hexaferrite, the magnetic and electrical properties enhance compared to simple barium hexaferrite and consequently they can be also an excellent candidate for such applications. For instance, they have a ferrimagnetic structure with a total magnetic moment of 20  $\mu\text{B}$  in the ground state [28–30]. Recently, were discovered in barium hexaferrites substituted by diamagnetic cations a large spontaneous polarization and multiferroic properties at room temperature. Furthermore, the remarkable magneto-electric characteristics of M-type hexaferrites are observed at room temperature that fabricated by a modified ceramic technique [31–33].

Previous reports on the synthesis of undoped and doped BFO samples by solid-state reaction route indicate that they have deficiency oxygen and Bi evaporation during preparation [34]. Moreover, when A site in perovskite structure was substituted by divalent cations, the charge balance in compound may have changed. These factors were caused the creation of oxygen vacancy, impurities, and unbalanced compound [35–37]. The presence of oxygen vacancy decreases a fraction of the oxidation degree of 3d ions to a lower value. This mechanism can be affected by total magnetic moment and the Curie temperature via the change of super exchange interaction strength [38, 39]. The substitution of trivalent rare-earth (RE = La, Nd, ..., and Y) ions in Bi site decreases impurity and oxygen vacancy [10, 40, 41]. Furthermore, the chemical methods of synthesis decrease Bi evaporation and oxygen loss. There are many chemicals routs such as sol–gel, sol–gel autocombustion, hydrothermal, and co-precipitation for preparing of various magnetic materials nanoparticle [35, 36, 42–44].

In the previous studies, it was observed that physical properties such as magnetic, electrical, and piezoelectric properties are strongly affected in various structural phases of  $\text{Bi}_{1-x}\text{La}(\text{RE})_x\text{FeO}_3$  compounds [10–13]; however, there is no reliable information on photocatalytic behavior at the MPB. In this work, we first prepared  $\text{BiFeO}_3$  and  $\text{Bi}_{0.83-x}\text{La}_{0.17}\text{Y}_x\text{FeO}_3$  ( $x = 0.0, 0.05, 0.10, 0.15$ , and 0.20)

nanoparticles by sol–gel method and studied their structural evolution. Finally, their magnetic properties and especially photocatalytic activity across the structural phase transitions investigated.

## 2 Experimental methods

The nanoparticles of  $\text{BiFeO}_3$  (BFO) and  $\text{Bi}_{0.83-x}\text{La}_{0.17}\text{Y}_x\text{FeO}_3$  ( $\text{BLY}_x\text{FO}$  NPs,  $x = 0.0, 0.05, 0.10, 0.15$  and 0.20) were prepared by the sol–gel technique, which the details of synthesis route were reported in our previous work [37]. High purity nitrates containing  $\text{Bi}(\text{NO}_3)_3 \cdot 5\text{H}_2\text{O}$ ,  $\text{La}(\text{NO}_3)_3 \cdot 9\text{H}_2\text{O}$ ,  $\text{Y}(\text{NO}_3)_3 \cdot 6\text{H}_2\text{O}$ , and  $\text{Fe}(\text{NO}_3)_3 \cdot 9\text{H}_2\text{O}$  in a stoichiometric molar ratio were dissolved in a  $\text{HNO}_3$  solution. After that, the tartaric acid was added as complexation.

The structural analysis was evaluated by X-ray diffraction (XRD) and Fullprof program. The microstructural properties were investigated by field-emission scanning electron microscopy (FE-SEM) method. The magnetic properties were performed by vibration sample magnetometer (VSM) analysis under applied magnetic fields up to 20 kOe at 300 K. The optical properties were measured by diffuse reflectance spectra (DRS) using Avantes spectrometer (Model: Avaspec-2048-TEC with Ava Lamp DH-S Setup) at room temperature. The photocatalytic activity test is studied by the degradation of methyl orange (MO) under visible light of 150 W mercury lamp. Here in, 100 mg catalyst was added to 5 mg/L of MO solution in an immersed well reactor under magnetic stirring at room temperature. Before illumination, the solution with catalyst is stirred for 30 min to attain absorption and desorption equilibrium. During the experiment, 2 mL of dye is taken out regular intervals and centrifuged to remove the catalyst. The concentration of MO was measured using UV–visible spectrophotometer (Varian Cary Bio 50 model). The degradation is calculated from relation  $C_t/C_0$  where  $C_0$  is the primary concentration at start the reaction and  $C_t$  is the concentration at time  $t$ .

## 3 Results and discussion

Figure 1a–c displays XRD pattern of BFO and  $\text{BLY}_x\text{FO}$  NPs at the room temperature. It is clear that all nanoparticles are approximately single phase. However, a small amount of  $\text{Bi}_2\text{O}_3$  and  $\text{YO}_{1.458}$  phases corresponding to the JCPDS files no. 01-074-1374 and 00-039-1063 are observed in BFO and  $\text{BLY}_0\text{FO}$  samples, respectively. These were demonstrated by (@) and (&) symbols in the XRD patterns of BFO and  $\text{BLY}_0\text{FO}$  NPs, respectively. If one considers the Fig. 1a–c carefully, the two characterizations are visible. First, the peaks at the same diffraction angle ( $2\theta$ ) in XRD patterns shift gradually toward higher  $2\theta$  with substituting  $\text{La}^{3+}$  and

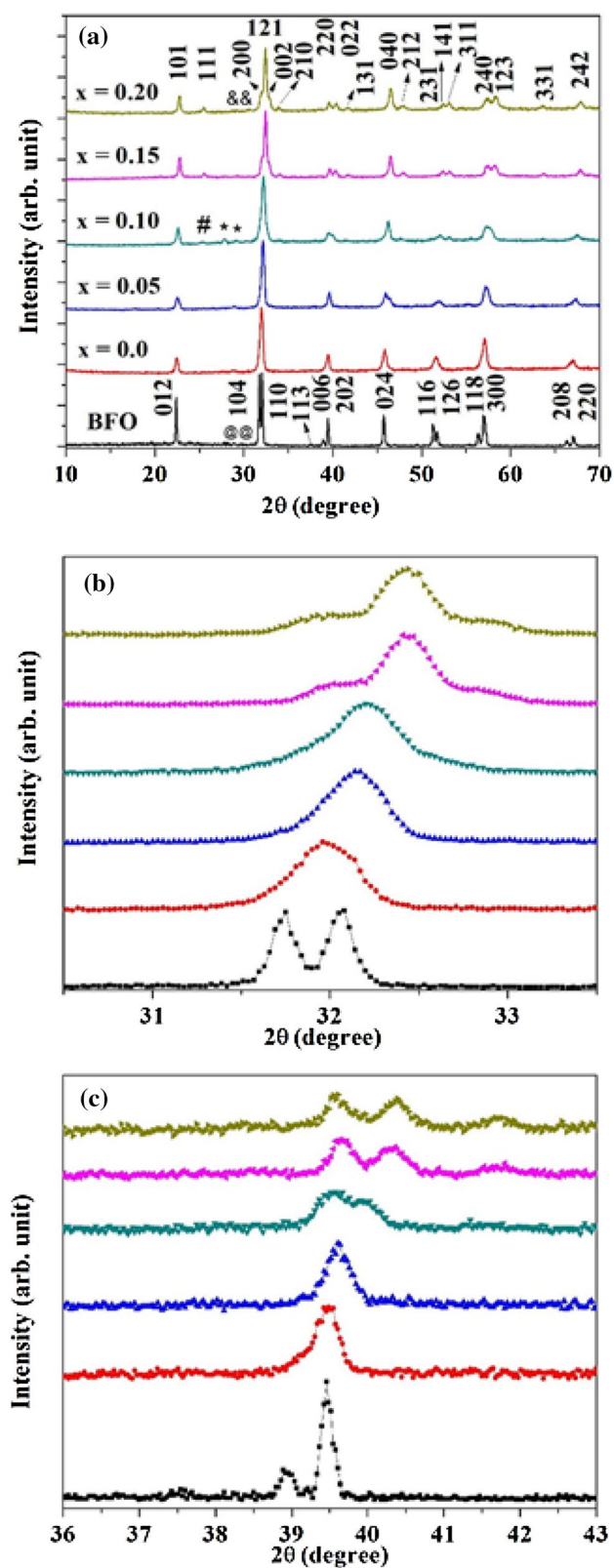


**Fig. 1** a The XRD patterns, and b, c the enlarged XRD patterns for BFO and  $\text{BLY}_x\text{FO}$  compounds

$\text{Y}^{3+}$ . According to the Bragg's law, this implies that the unit cell volume decreases. Second, while doublet peaks in BFO merge to single peaks in sample with  $x=0$ , themselves split into doublet or triplet peaks in samples with  $x=0.15$  and  $0.20$ , again. On the other hand, the new peaks are emerged in XRD patterns with increasing  $\text{La}^{3+}$  and  $\text{Y}^{3+}$  substitution that were indicated with symbols (\*) and (#). Furthermore, the appearance of new peaks by symbol (\*) in  $x=0$  grows slowly in samples with  $x=0.05$  and  $0.10$ , and then disappear in  $x=0.20$ . This trend indicates that we deal with multist-structure phase transition in  $\text{BLY}_x\text{FO}$  samples. Such behavior was observed in several previous reports [10, 11, 45]. To obtain the crystal structure information of BFO and  $\text{BLY}_x\text{FO}$  NPs such as the lattice parameters, coexistence phases and phase percentages were used Fullprof software. For running Fullprof program, the lattice constants and atomic positions of BFO [46],  $\text{PbZrO}_3$  [47], and  $\text{LaFeO}_3\text{-YFeO}_3$  [48] for R3c, Pbam, and Pnma space groups were used as input data, respectively. Figure 2a displays the Rietveld refinement of XRD pattern for BFO sample with R3c space group. However, the result of Rietveld refinement with R3c space group for  $\text{BLY}_0\text{FO}$  sample was not satisfied. The existence of peaks with (\*) symbol confirms that the orthorhombic phase with Pbam space group contributes in this sample [19]. This result is consistent with phase evolution of  $\text{Bi}_{1-x}\text{La}_x\text{FeO}_3$  system [10, 11]. Therefore, the XRD pattern of  $\text{BLY}_0\text{FO}$  refined simultaneously by two space groups of R3c and Pbam, as exhibited in Fig. 2b. Starting  $\text{Y}^{3+}$  substitution in  $\text{BLY}_0\text{FO}$  sample, the contribution of R3c phase strongly suppressed and crystal structure can be successfully described as the mixture of Pbam and Pnma phases in the concentration range of  $x \leq 0.15$  (see Fig. 2c). Finally, with increasing  $\text{Y}^{3+}$  content ( $x=0.20$ ), the crystal structure was refined only with Pnma space group, as shown in Fig. 2d. This trend is very comparable to that of  $\text{Bi}_{0.8}\text{La}_{0.2-x}\text{Pr}_x\text{FeO}_3$  compounds [11].

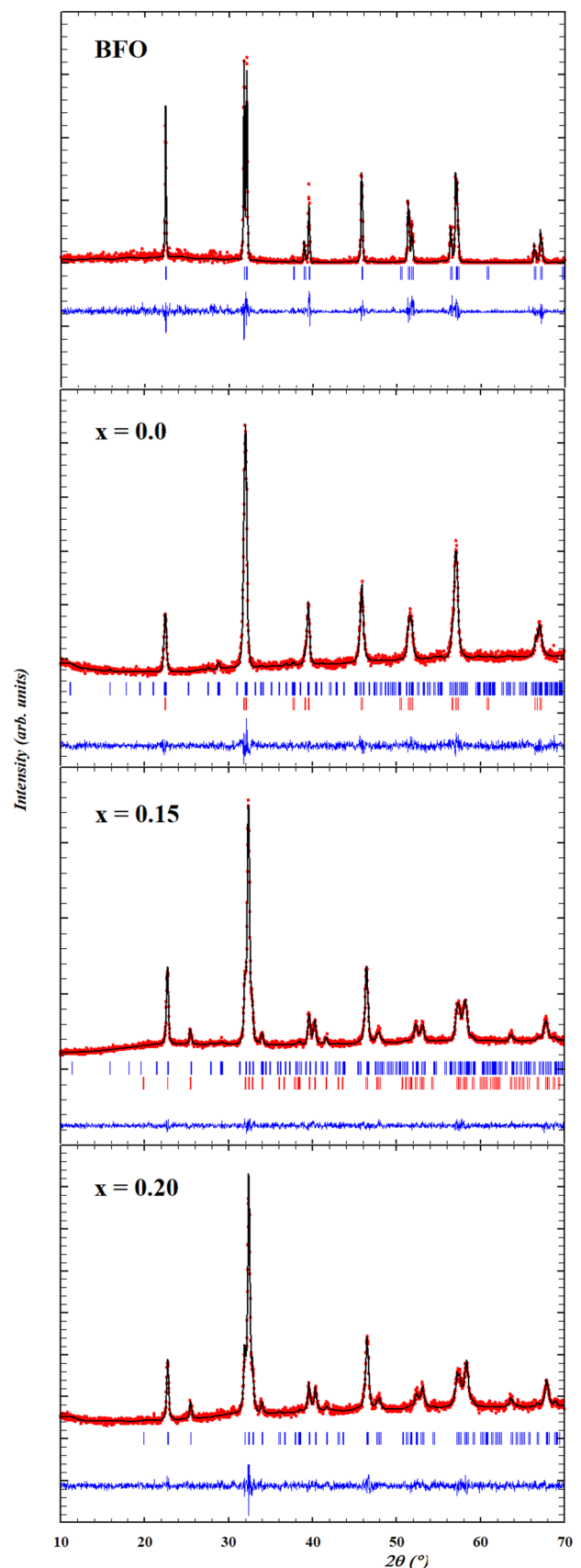
Unlike hexaferrite ( $\text{BaFe}_{12}\text{O}_{19}$ ) and spinel ferrite ( $\text{MFe}_2\text{O}_4$ , M is a divalent or trivalent cations) structure, the number of atomic sites is equal to 1 for A and B cations in perovskite structure with R3c and Pnma space groups. Therefore,  $\text{La}^{3+}$  and  $\text{Y}^{3+}$  cations occupy only the related Bi site [49–51]. In addition, the Rietveld refinement parameters of BFO and  $\text{BLY}_x\text{FO}$  sample are summarized in Table 1. Since, the unit cell volume is different in the various phase of  $\text{ABO}_3$  perovskite structure, the unit cell volume per  $\text{ABO}_3$  formula is defined as  $v = V/z$ , where  $z$  is the number of  $\text{ABO}_3$  formula in every unit cell [51]. Table 1 shows the doping  $\text{La}^{3+}$  and  $\text{Y}^{3+}$  ions with smaller ionic radius respect to that of  $\text{Bi}^{3+}$  lead to decreasing  $v$ . Finally, the X-ray pattern of the BFO and  $\text{BLY}_{0.2}\text{FO}$  samples was indexed based on R3c and pnm space groups, respectively.

Figure 3 presents the FE-SEM micrographs of  $\text{BLY}_x\text{FO}$  NPs with  $x=0.0, 0.10, \text{ and } 0.20$ . It is clear that the

**Fig. 2** The Rietveld refinement of XRD analysis for BFO,  $x=0.0$ , 0.15, and 0.20 with R3c, R3c+Pbam, Pbam+Pnma, Pnma models, respectively

distribution of particles size is almost uniform and less than 100 nm. Comparing the images, it can be deduced that the average nanoparticle size decrease slightly with increasing  $Y^{3+}$  content. It means that with increasing rate of crystallization process in grains with  $Y^{3+}$  substitution under the same thermal treatment condition for sample with  $Y^{3+}$ -free. Furthermore, to confirm the elemental concentration in  $BLY_xFO$  NPs, the energy-dispersive X-ray (EDAX) analysis was performed. The EDAX spectrum of corresponding FE-SEM images is shown in Fig. 4. The results demonstrate that samples only consist of Bi, La, Y, Fe, and O elements and the mole ratio of Bi:Y in  $BLY_xFO$  NPs is  $0.8-x:x$ , that of Fe:O:La = 1:1:0.2 is almost constant.

The magnetic hysteresis loops of BFO and  $BLY_xFO$  NPs are shown in Fig. 5. It is obvious that while BFO displays an antiferromagnetic treatment, other samples have a weak ferromagnetism behavior. Among them, sample with  $x=0.0$  is exhibited the highest remnant magnetisation ( $M_r$ ) and coercive field ( $H_c$ ). Moreover, with increasing  $Y^{3+}$  content up to  $x=0.10$ , both  $M_r$  and  $H_c$  decrease, and then enhance in sample with  $x=0.15$ , and finally decrease in  $x=0.20$  sample, again. These results are a common feature in  $Bi_{1-x}RE_xFeO_3$  compounds [12, 52–54]. Since,  $Y^{3+}$  and  $La^{3+}$  ions have no magnetic moment, thus magnetic behavior is only due to Fe ion sublattice [53]. On the other hand, Fe ion concentration is equal in all samples, and therefore, the difference in the magnetic behavior of studied samples is the result of different  $FeO_6$  octahedra distortion by various doping levels. The strength of super exchange interaction strongly depends on the Fe–O–Fe bond angle in  $FeO_6$  octahedra. Previous reports on the magnetic properties of  $Bi_{1-x}RE_xFeO_3$  compounds indicate that the highest ferromagnetism behavior occurs in the intersection region of rhombohedral and orthorhombic phases [12, 53–55]. In this region, not only the SCSS is suppressed but also the Fe–O–Fe bond angle is reduced [55]. In the sample with  $x=0$  because of both decreasing rhombohedral phase percent (66%) and Fe–O–Fe bond angle compared to that of BFO, the weak ferromagnetism behavior observes in this compound. In other compounds with orthorhombic structure, there is not the spiral spin structure and it is completely destroyed. Therefore, only  $FeO_6$  octahedra distortion can be affected magnetic feature. For instance, increasing Fe–O–Fe for Pbam phase in  $x=0.05$  compared to that of the orthorhombic phase of  $x=0$  sample is caused reducing of  $M$  and  $M_r$ . This postulate explain enhancing the weak ferromagnetism behavior for sample with  $x=0.15$  compared to that of  $x=0.10$  and 0.20, based on Fe–O–Fe data for Pnma phase in Table 1. Finally, the magnetic parameters obtained from the  $M-H$  loops are listed in Table 2.



**Table 1** The crystal structure parameters for BFO and BLY<sub>x</sub>FO compounds derived by the Rietveld refinement of XRD analysis

Sample	<i>a</i> (Å)	<i>b</i> (Å)	<i>c</i> (Å)	<i>V</i> (Å <sup>3</sup> )	<i>c/a</i>	<i>Z</i>	<i>v</i> (Å <sup>3</sup> )	% phase	Fe–O–Fe	<i>R</i> <sub>wp</sub>	<i>R</i> <sub>p</sub>	GOF
BFO	5.576(4)	5.576(4)	13.866(9)	373.444	2.487	6	62.24	100	161.5	22.2	15.7	1.31
<i>x</i> =0 R3c	5.580(4)	5.580(4)	13.776(8)	371.551	2.469	6	61.92	66.6	156.2	8.57	6.66	1.21
<i>x</i> =0 pbam	5.578(3)	7.929(5)	11.177(6)	494.421	2.004	8	61.80	33.4	109.6, 131.2 148.3, 175.3 124.7 <sup>a</sup>	8.57	6.66	1.15
<i>x</i> =0.05 pbam	5.553(9)	7.914(5)	11.134(0)	489.419	2.005	8	61.18	71.1	138.8, 144.7 152.6, 146.1 163.38	6.95	5.45	1.12
<i>x</i> =0.05 pnma	5.571(8)	5.599(5)	7.827(7)	244.221	1.405	4	61.05	28.9	–	6.95	5.45	1.23
<i>x</i> =0.10 pbam	5.506(7)	7.834(2)	11.186(8)	482.612	2.031	8	60.33	57.2	–	6.47	5.04	1.15
<i>x</i> =0.10 pnma	5.509(6)	5.590(7)	7.839(5)	241.479	1.423	4	60.37	42.8	163.7, 173.7 <sup>a</sup>	6.47	5.04	1.17
<i>x</i> =0.15 pbam	5.464(1)	7.819(0)	11.192(6)	478.199	2.048	8	59.77	18.6	–	5.08	4.01	1.33
<i>x</i> =0.15 pnma	5.463(8)	5.599(1)	7.820(3)	239.239	1.431	4	59.81	81.4	132.0, 157.0	5.08	4.01	1.20
<i>x</i> =0.20 pnma	5.450(1)	5.603(6)	7.804(4)	238.349	1.432	4	59.59	100	131.1, 165.3	6.85	5.45	1.21

<sup>a</sup>There are five (two) different bond angles in orthorhombic structure with Pbam (Pnma) space group

To study the optical properties of BFO and BLY<sub>x</sub>FO NPs, the UV–Vis diffuse reflectance spectra (DRS) were carried out in 100–1200 nm wavelength. Figure 6 shows the adsorption [*F*(*R*)] spectra of all compounds that were calculated using Kabelka–Munk (K–M) formula [56]. For instance, the [*F*(*R*)/*hν*]<sup>2</sup> versus *hν* (photon energy) curve for sample with *x*=0.05 were observed the inset of Fig. 6. Using such plotted curve for all compounds, the direct band gap of BFO and BLY<sub>x</sub>FO NPs (*x*=0.0, 0.05, 0.10, 0.15, 0.20) was determined about 2.03, 1.93, 2.05, 2.07, 2.09, and 2.10 eV, respectively. It is clear that while the band gap decreases with substituting La ion in BFO, it increases with doping Y ion in BLY<sub>0</sub>FO compound. These results are agreement with literature data [22, 57–59]. It is generally known that the band gap in REFeO<sub>3</sub> (RE=rare earth and Bi) is originated from overlap of Fe-3d and O-2p orbitals [1]. In addition, the change in particle size, morphology, and lattice constants of undoped and doped BFO can be affected the band gap [58]. It should be noted that the thermal treatment for synthesizing our compounds is similar, thus as shown in Fig. 3, it can be approximately assumed that the particle size and morphology of studied compounds are almost equal together. On the other hand, a comparison between the variations of *c/a* parameter and *E<sub>g</sub>* of our samples indicated that increasing (decreasing) of *c/a* in rhombohedral (orthorhombic) phase are corresponding to decreasing (increasing) of *E<sub>g</sub>*. Such result is also reported in Ref. [58].

The photocatalytic activity of the BFO and BLY<sub>x</sub>FO NPs is evaluated by degradation of typical organic contaminant MO under visible light at pH value 2 and 0.5 mL H<sub>2</sub>O<sub>2</sub>, and the time-dependent photodegradation of MO is illustrated in Fig. 6a. At the first step, degradation is tested in the stability of MO dye that called photolysis (without any catalyst). After 120 min, the degradation efficiency of MO is

negligible. In next step, the photocatalytic activities of MO are performed for BFO and BLY<sub>x</sub>FO NPs. The photocatalytic process for the degradation of MO can be described as having begun in the radiation effects of catalyst excitation irradiation is continued through the formation of electron–hole pairs at the catalyst surface. The hole, due to its high oxidation potential, can convert the MO into a reactive intermediate compound. Another intermediate compound is ·OH radical which can increase the separation of electron–hole and destroy the MO dye [59]. Therefore, H<sub>2</sub>O<sub>2</sub> can generate ·OH radicals by dissociation or photo-fenton reaction [60]. The BFO surfaces positive charge at pH value 2 (at pH < 6.7, the isoelectric point of BFO) and MO is bunch of azo anionic dyes, so it is well adsorbed in the acidic solution by the catalyst surface and catalytic activity is progressing [61].

It is clear in Fig. 7a, and the degradation of MO for BFO and BLY<sub>x</sub>FO NPs is 52, 76, 95, 41, 63, and 100%, respectively. Therefore, the type and amount of RE (La and Y) ion concentration plays a significant role in the degradation of the MO dye. It is generally known that the photocatalytic activity in BFO family is depending on many factors such as morphology, particle size, and band gap and structure [62, 63]. Our results indicate that the degradation of MO with sample with *x*=0 increases compared to BFO sample. According to finding of our optical measurements, this enhancement can be due to decreasing *E<sub>g</sub>* with La substitution as reported previously [22]. Moreover, based on our structural investigations, the phase boundary between rhombohedral polar and orthorhombic non-polar structure starts in this sample. The presence of a mixture structure can affect the photocatalytic activity in doped BFO, as well [21, 22]. On the other hand, the variation of degradation of MO for Y-doped BLY<sub>x</sub>FO samples is very complicated

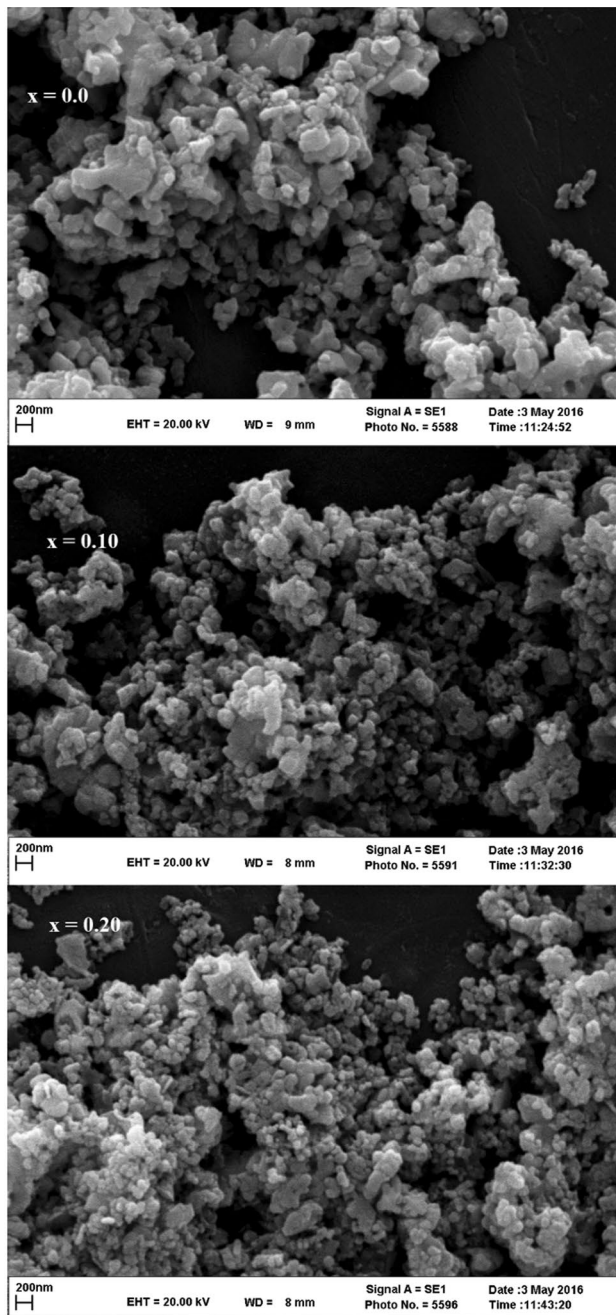


**Fig. 3** The FE-SEM images of BLY<sub>x</sub>FO compounds for  $x=0.0$ , 0.10, and 0.20

and ambiguous. While photocatalyst activity increases for sample with  $x=0.05$ , but degradation of MO strongly decreases for  $x=0.10$ , and then, it enhances with more Y doping, again. As it was mentioned before, the morphology of studied samples is similar together. Furthermore, previous report on the size particle effect on photocatalyst activity of BFO exhibits that the particles size in the range of 50–100 nm has only 5% difference in photocatalyst activity [62]. Therefore, the reduction of photocatalyst activity for

$x=0.10$  sample compared to samples with  $x=0.05$  and 0.15 cannot be due to morphology and size effects. On the other hand, according to the optical results, the  $E_g$  increases with Y doping. Therefore, decreasing of photocatalyst activity for  $x=0.10$  may be attributed to increasing  $E_g$ . Moreover, as another possibility, the presence of equal mixed-phase of anti-polar (pbam) and non-polar (pnma) may be influenced on decreasing of photocatalyst activity in  $x=0.10$  sample. Finally, with increasing of non-polar phase contribution by more doping Y ion, the photocatalyst activity increases and is maximum in sample with  $x=0.20$ .

The kinetic behavior between dye molecules and photocatalyst is shown by the Langmuir model (based on Eq. 1). The model is used to determine the relationship between the apparent constant of the pseudo-first-order reaction rate and the initial concentration of the organic dye [64]. As shown in Fig. 7, the photodegradation of MO is followed by Eq. (1) of the pseudo-first-order kinetics equation:

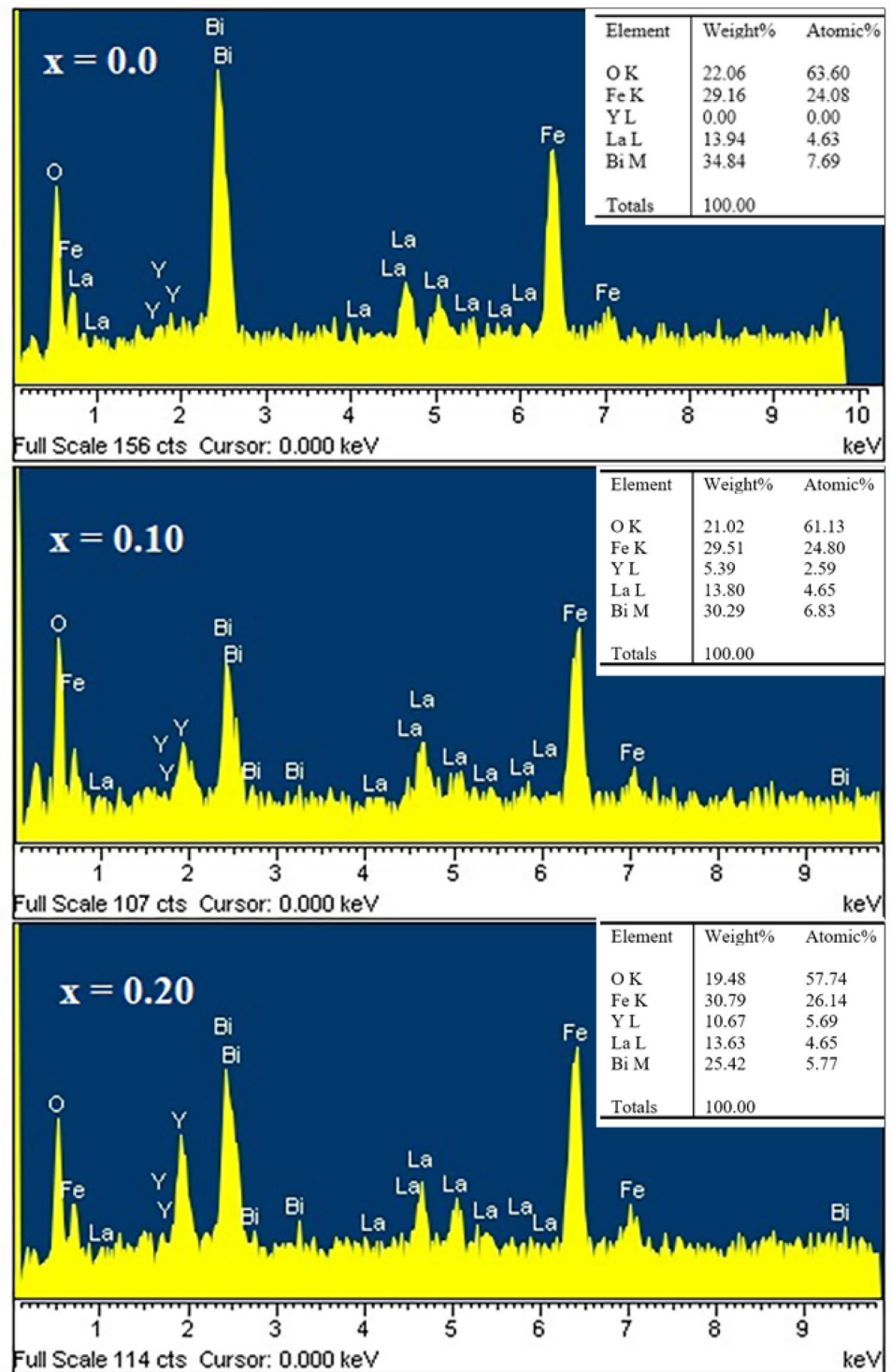
$$\ln C_t/C_0 = -K_{app}t, \quad (1)$$

where  $C_t$  and  $C_0$  are the concentration at time  $t$ , and zero time, respectively, and  $K_{app}$  is the pseudo-first-order rate apparent constant. The rate constants obtained for BFO and BLY<sub>x</sub>FO NPs are shown in Fig. 6c.

## 4 Conclusion

In summary, we have successfully synthesized BFO and BLY<sub>x</sub>FO NPs by tartaric acid sol–gel route. The Rietveld refinement of XRD analysis confirms a serial phase transition of R3c–Pbam–pnma as a morphotropic phase boundary in these compounds. Doping La<sup>3+</sup> and Y<sup>3+</sup> ions with smaller ionic radius respect to that of Bi<sup>3+</sup> leads to decreasing the unit cell volume per formula unit. The morphology and particles size of BLY<sub>x</sub>FO NPs were estimated by FE-SEM images. It is founded that the distribution of particles size is almost uniform and less than 100 nm. While BFO displays an antiferromagnetic treatment, other samples indicate a weak ferromagnetism behavior. The sample with  $x=0.0$  is exhibited the highest remnant magnetisation ( $M_r=0.09$  emu/g) and coercive field ( $H_c=5414$  Oe). The band gap of BFO and BLY<sub>x</sub>FO NPs ( $x=0.0$ , 0.05, 0.10, 0.15, 0.20) were determined about 2.03, 1.93, 2.05, 2.07, 2.09, and 2.10 eV, respectively. The photocatalytic activity of the BFO and BLY<sub>x</sub>FO NPs is evaluated by degradation of typical organic contaminant MO under visible light at pH value 2 and 0.5 mL H<sub>2</sub>O<sub>2</sub>. The results indicate that with increasing La doping concentration from 0 to 17% in BFO, the degradation of MO enhances from 52 to 76%. The photocatalytic activity dependence on Y concentration has a behavior more complicated, while the

**Fig. 4** The EDAX spectrum of  $\text{Bi}_{0.83-x}\text{La}_{0.17}\text{Y}_x\text{FeO}_3$  compounds for  $x=0.0$ , 0.10, and 0.20



photocatalytic activity for  $x=0.05$  and 0.20 samples is 95 and 100% respectively, but for  $x=0.10$  and 0.15 samples

are 41 and 63%, respectively. These compounds with the MPB characterization can be considered as practical functionalities.

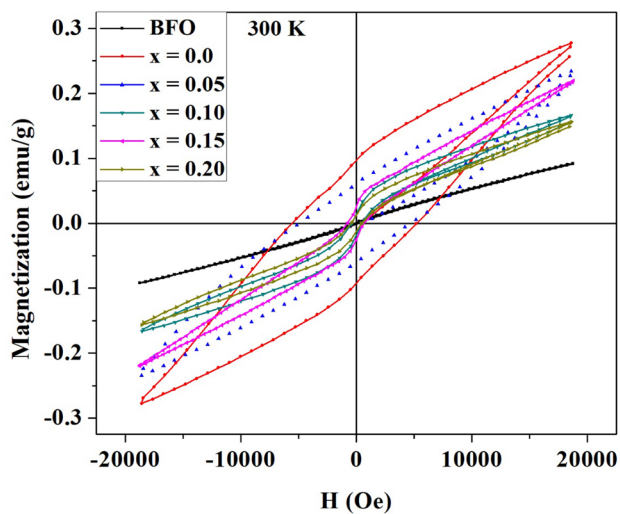


Fig. 5 The M–H hysteresis loop for BFO and BLY<sub>x</sub>FO compounds

**Table 2** The magnetic parameters for BFO and BLY<sub>x</sub>FO compounds

Sample	<i>M</i> (emu/g) at 20 kOe	<i>M<sub>r</sub></i> (emu/g)	<i>H<sub>c</sub></i> (Oe)
BFO	0.09	$7 \times 10^{-4}$	107
<i>x</i> =0.0	0.27	0.090	5414
<i>x</i> =0.05	0.23	0.060	4803
<i>x</i> =0.10	0.16	0.012	325
<i>x</i> =0.15	0.21	0.029	665
<i>x</i> =0.20	0.15	0.010	404

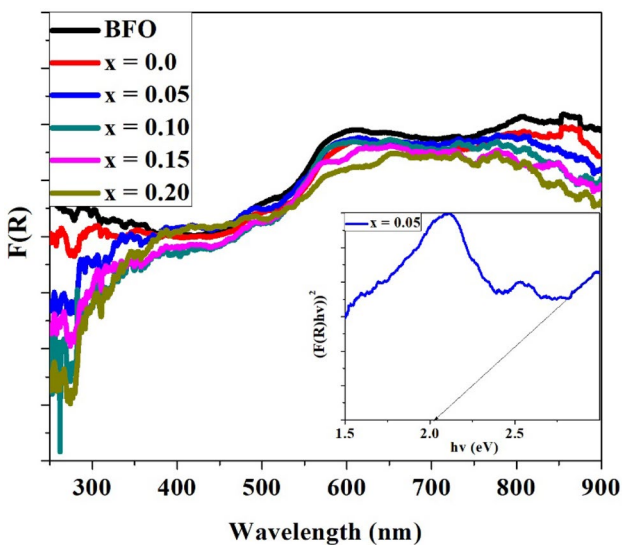


Fig. 6 Diffused reflectance spectra for BFO and BLY<sub>x</sub>FO compounds (inset shows band gap for *x*=0.05)

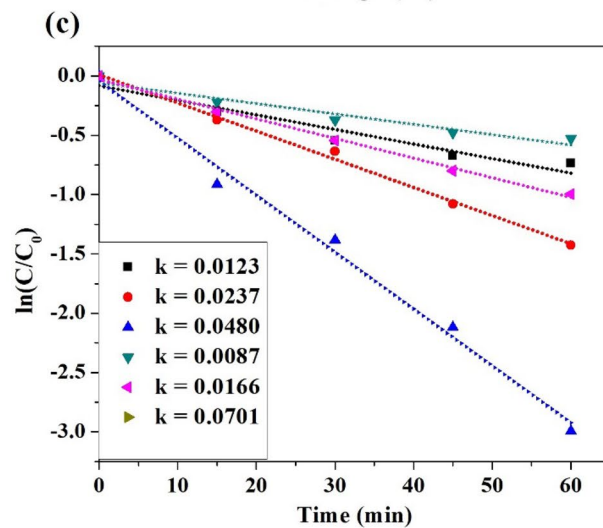
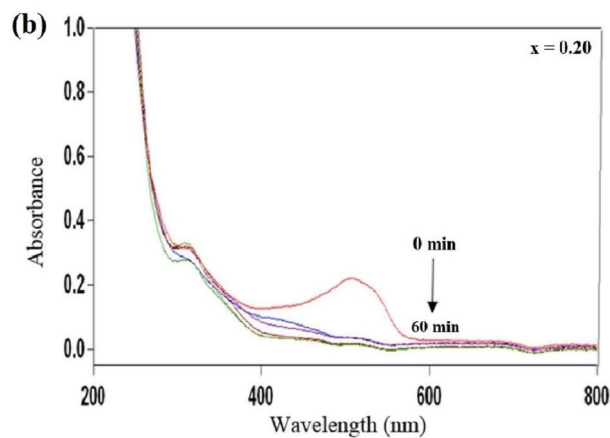
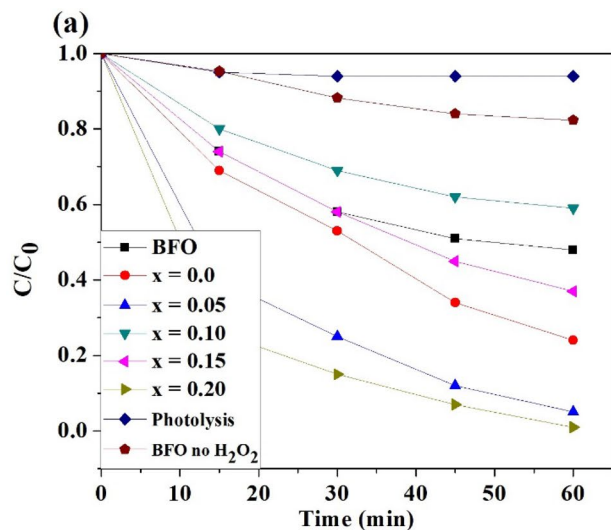


Fig. 7 a Photocatalytic degradation efficiencies of photolysis, BFO, and BLY<sub>x</sub>FO compounds to degrade MO. b The degradation graph of MO in *x*=0.20 sample. c Photodegradation kinetics of BFO and BLY<sub>x</sub>FO compounds



**Acknowledgements** This work has been supported by research contract of the Islamic Azad University's Mashhad, Iran under Grant no. 510-92490/302/72.

## References

- G. Catalan, J.F. Scott, Physics and applications of bismuth ferrite. *Adv. Mater.* **21**, 2463 (2009)
- R. Haumont, I.A. Kornev, S. Lisenkov, L. Bellaiche, J. Kreisel, B. Dkhil, Phase stability and structural temperature dependence in powdered multiferroic  $\text{BiFeO}_3$ . *Phys. Rev. B* **78**, 134108 (2008)
- S.M. Wu, S.A. Cybart, P. Yu, M.D. Rossell, J.X. Zhang, R. Ramesh, R.C. Dynes, Reversible electric control of exchange bias in a multiferroic field-effect device. *Nat. Mater.* **9**, 756 (2010)
- R. Mazumder, P. Sujatha Devi, Dipten Bhattacharya, P. Choudhury, A. Sen, M. Raja, Ferromagnetism in nanoscale  $\text{BiFeO}_3$ . *Appl. Phys. Lett.* **91**, 062510 (2007)
- A.K. Pradhan, K. Zhang, D. Hunter, J.B. Dadson, G.B. Loutts, P. Bhattacharya, R. Katiyar, J. Zhang, D.J. Sellmyer, U.N. Roy, Y. Cui, A. Burger, Magnetic and electrical properties of single-phase multiferroic  $\text{BiFeO}_3$ . *J. Appl. Phys.* **97**, 093903 (2005)
- H. Shu, Z. Wang, W. Mao, Y. Ma, L. Chu, X. Wang, W.W. Chen, J. Zhang, J. Yang, R. Song, X. Li, Enhanced multiferroic properties of (Nd, Cr) co-doped  $\text{BiFeO}_3$  nanoparticles. *Appl. Phys. A* **123**, 338 (2017)
- G.L. Song, G.J. Ma, J. Su, T.X. Wang, H.Y. Yang, F.G. Chang, Effect of  $\text{Ho}^{3+}$  doping on the electric, dielectric, ferromagnetic properties and  $T_C$  of  $\text{BiFeO}_3$  ceramics. *Ceram. Int.* **40**, 3579 (2014)
- S. Karimi, I.M. Reaney, I. Levin, I. Sterianou, Nd-doped  $\text{BiFeO}_3$  ceramics with antipolar order. *Appl. Phys. Lett.* **94**, 112903 (2009)
- S. Fujino, M. Murakami, V. Anbusathaiah, S.H. Lim, V. Nagarajan, C.J. Fennie, M. Wuttig, L. Salamanca-Riba, I. Takeuchi, Combinatorial discovery of a lead-free morphotropic phase boundary in a thin-film piezoelectric perovskite. *Appl. Phys. Lett.* **92**, 202904 (2008)
- I.O. Troyanchuk, D.V. Karpinsky, M.V. Bushinsky, V.A. Khomchenko, G.N. Kakazei, J.P. Araujo, M. Tovar, V. Sikolenko, V. Efimov, A.L. Kholkin, Isothermal structural transitions, magnetization and large piezoelectric response in  $\text{Bi}_{1-x}\text{La}_x\text{FeO}_3$  perovskites. *Phys. Rev. B* **83**, 054109 (2011)
- D.V. Karpinsky, I.O. Troyanchuk, O.S. Mantyskaya, V.A. Khomchenko, A.L. Kholkin, Structural stability and magnetic properties of  $\text{Bi}_{1-x}\text{La}(\text{Pr})_x\text{FeO}_3$  solid solutions. *Solid State Commun.* **151**, 1686 (2011)
- X. Chen, G. Hu, W. Wu, C. Yang, X. Wang, Large piezoelectric coefficient in Tb-doped  $\text{BiFeO}_3$  films. *J. Am. Ceram. Soc.* **93**, 948 (2010)
- S.B. Emery, C.J. Cheng, D. Kan, F.J. Rueckert, S.P. Alpay, V. Nagarajan, I. Takeuchi, B.O. Wells, Phase coexistence near a morphotropic phase boundary in Sm-doped  $\text{BiFeO}_3$  films. *Appl. Phys. Lett.* **97**, 152902 (2010)
- Kumar Nitin, Shukla Alok, R.N.P. Choudhary, Structural, electrical and magnetic properties of (Cd, Ti) Modified  $\text{BiFeO}_3$ . *Phys. Lett. A* **381**, 2721 (2017)
- N. Kumar, A. Shukla, R.N.P. Choudhary, Structural, electrical and magnetic characteristics of Ni/Ti modified  $\text{BiFeO}_3$  lead free multiferroic material. *J. Mater. Sci. Mater. Electron.* **28**, 6673 (2017)
- N. Kumar, A. Shukla, R.N.P. Choudhary, Development of lead-free multifunctional materials  $\text{Bi}(\text{Co}_{0.45}\text{Ti}_{0.45}\text{Fe}_{0.10})\text{O}_3$ . *Prog. Nat. Sci. Mater. Int.* **28**, 308–314 (2018)
- N. Kumar, A. Shukla, N. Kumar, R.N.P. Choudhary, A. Kumar, Structural, electrical and multiferroic characteristics of lead-free multiferroics:  $\text{Bi}(\text{Co}_{0.5}\text{Ti}_{0.5})\text{O}_3$ – $\text{BiFeO}_3$  solid solution. *RSC. Adv.* **8**, 36939 (2018)
- N. Kumar, A. Shukla, R.N.P. Choudhary, Structural, dielectric, electrical and magnetic characteristics of lead-free multiferroics:  $\text{Bi}(\text{Cd}_{0.5}\text{Ti}_{0.5})\text{O}_3$ – $\text{BiFeO}_3$  solid solution. *J. Alloys. Compd.* **747**, 895 (2018)
- V.A. Khomchenko, L.C.J. Pereira, J.A. Paixao, Substitution-driven structural and magnetic phase transitions in  $\text{Bi}_{0.86}(\text{La}, \text{Sm})_{0.14}\text{FeO}_3$  system. *J. Phys. D Appl. Phys.* **44**, 185406 (2011)
- V.A. Khomchenko, V.V. Shvartsman, P. Borisov, W. Kleemann, D.A. Kiselev, I.K. Bdikin, J.M. Vieira, A.L. Kholkin, Crystal structure and magnetic properties of  $\text{Bi}_{0.8}(\text{Gd}_{1-x}\text{Ba}_x)_{0.2}\text{FeO}_3$  ( $x = 0, 0.5, 1$ ) multiferroics. *J. Phys. D Appl. Phys.* **42**, 045418 (2009)
- R. Guo, L. Fang, W. Dong, F. Zheng, M. Shen, Enhanced photocatalytic activity and ferromagnetism in Gd doped  $\text{BiFeO}_3$  nanoparticles. *J. Phys. Chem. C* **114**, 21390 (2010)
- R. Dhanalakshmi, M. Muneeswaran, K. Shalini, N.V. Giridharan, Enhanced photocatalytic activity of La-substituted  $\text{BiFeO}_3$  nanostructures on the degradation of phenol red. *Mater. Lett.* **165**, 205 (2016)
- Z. Hu, D. Chen, S. Wang, N. Zhang, L. Qin, Y. Huang, Facile synthesis of Sm-doped  $\text{BiFeO}_3$  nanoparticles for enhanced visible light photocatalytic performance. *J. Mater. Sci. Eng. B* **220**, 1 (2017)
- P.R. Vanga, R.V. Mangalaraja, M. Ashok, Effect of co-doping on the optical, magnetic and photocatalytic properties of the Gd modified  $\text{BiFeO}_3$ . *J. Mater. Sci. Mater. Electron.* **27**, 5699 (2016)
- S.V. Trukhanov, A.V. Trukhanov, V.G. Kostishyn, L.V. Panina, V. Trukhanov An, V.A. Turchenko, D.I. Tishkevich, E.L. Trukhanova, O.S. Yakovenko, Matzui L. Yu, Investigation into the structural features and microwave absorption of doped barium hexaferrites. *Dalton Trans.* **46**, 9010 (2017)
- S.V. Trukhanov, A.V. Trukhanov, V.G. Kostishyn, L.V. Panina, V. Trukhanov An, V.A. Turchenko, D.I. Tishkevich, E.L. Trukhanova, O.S. Yakovenko, L.Y. Matzui, D.A. Vinnik, D.V. Karpinsky, Effect of gallium doping on electromagnetic properties of barium hexaferrite. *J. Phys. Chem. Solid* **111**, 142 (2017)
- S.V. Trukhanov, A.V. Trukhanov, L.V. Panina, V.G. Kostishyn, V.A. Turchenko, E.L. Trukhanova, V. Trukhanov An, T.I. Zubar, V.M. Ivanov, D.I. Tishkevich, D.A. Vinnik, S.A. Gudkova, D.S. Klygach, M.G. Vakhitov, P. Thakur, A. Thakur, Y. Yang, Temperature evolution of the structure parameters and exchange interactions in  $\text{BaFe}_{12-x}\text{In}_x\text{O}_{19}$ . *J. Magn. Magn. Mater.* **466**, 393 (2018)
- V.A. Turchenko, A.V. Trukhanov, I.A. Bobrikov, S.V. Trukhanov, A.M. Balagurov, Study of the crystalline and magnetic structures of  $\text{BaFe}_{11.4}\text{Al}_{0.6}\text{O}_{19}$  in a wide temperature range. *J. Surf. Investig.* **9**, 17 (2015)
- S.V. Trukhanov, A.V. Trukhanov, V.A. Turchenko, V.G. Kostishyn, L.V. Panina, I.S. Kazakevich, A.M. Balagurov, Structure and magnetic properties of  $\text{BaFe}_{11.9}\text{In}_{0.1}\text{O}_{19}$  hexaferrite in a wide temperature range. *J. Alloys. Compd.* **689**, 383 (2016)
- A.V. Trukhanov, V.G. Kostishyn, L.V. Panina, S.H. Jabarov, V.V. Korovushkin, S.V. Trukhanov, E.L. Trukhanova, Magnetic properties and Mossbauer study of gallium doped M-type barium hexaferrites. *Ceram. Int.* **43**, 12822 (2017)
- A.V. Trukhanov, L.V. Panina, S.V. Trukhanov, V.A. Turchenko, M. Salem, Evolution of structure and physical properties in Al-substituted Ba-hexaferrites. *Chin. Phys. B* **25**, 016102 (2016)
- A.V. Trukhanov, S.V. Trukhanov, V.G. Kostishyn, L.V. Panina, M.M. Salem, I.S. Kazakevich, V.A. Turchenko, V.V. Kochervinskii, D.A. Krivchenya, Multiferroic properties and structural features of M-type Al-substituted barium hexaferrites. *Phys. Solid State* **59**, 737 (2017)
- V. Turchenko, A. Trukhanov, S. Trukhanov, M. Balasoiu, N. Lupu, Correlation of crystalline and magnetic structures of barium

- ferrites with dual ferroic properties. *J. Magn. Magn. Mater.* **477**, 9 (2019)
34. Z.X. Cheng, A.H. Li, X.L. Wang, S.X. Dou, K. Ozawa, H. Kimura, S.J. Zhang, T.R. Shrout, Structure, ferroelectric properties, and magnetic properties of the La-doped bismuth ferrite. *J. Appl. Phys.* **103**, 07E507 (2008)
  35. M.A. Almessiere, Y. Slimani, H. Gungune, A. Bayka, S.V. Trukhanov, A.V. Trukhanov, Manganese/yttrium codoped strontium nanohexaferrites: evaluation of magnetic susceptibility and Mossbauer spectra. *Nanomaterials* **9**, 24 (2019)
  36. M.A. Almessiere, A.V. Trukhanov, Y. Slimani, K.Y. You, S.V. Trukhanov, E.L. Trukhanova, F. Esa, A. Sadaqat, K. Chaudhary, M. Zdorovets, A. Baykal, Correlation between composition and electrodynamic properties in nanocomposites based on hard/soft ferrimagnetics with strong exchange coupling. *Nanomaterials* **9**, 202 (2019)
  37. A.V. Khomchenko, D.A. Kiselev, J.M. Vieira, L. Jian, A.L. Kholkin, A.M.L. Lopes, Y.G. Pogorelov, J.P. Araujo, M. Maglione, Effect of diamagnetic Ca, Sr, Pb, and Ba substitution on the crystal structure and multiferroic properties of the BiFeO<sub>3</sub> perovskite. *J. Appl. Phys.* **103**, 024105 (2008)
  38. S.V. Trukhanov, I.O. Troyanchuk, I.M. Fita, H. Szymczak, K. Barner, Comparative study of the magnetic and electrical properties of Pr<sub>1-x</sub>Ba<sub>x</sub>MnO<sub>3-δ</sub> manganites depending on the preparation conditions. *J. Magn. Magn. Mater.* **237**, 276 (2001)
  39. S.V. Trukhanov, L.S. Lobanovski, M.V. Bushinsky, I.O. Troyanchuk, H. Szymczak, Magnetic phase transitions in the anion-deficient La<sub>1-x</sub>Ba<sub>x</sub>MnO<sub>3-x/2</sub> (0 ≤ x ≤ 0.50) manganites. *J. Phys. Condens. Matter* **15**, 1783 (2003)
  40. G.L. Yuan, S.W. Or, J.M. Liu, Z.G. Liu, Structural transformation and ferroelectromagnetic behavior in single-phase Bi<sub>1-x</sub>Nd<sub>x</sub>FeO<sub>3</sub> multiferroic ceramics. *J. Appl. Phys.* **89**, 052905 (2006)
  41. L. Luo, W. Wei, X. Yuan, K. KaiShen, M. Xu, Q. Xu, Multiferroic properties of Y-doped BiFeO<sub>3</sub>. *J. Alloys. Compd.* **540**, 36 (2012)
  42. A.S. Naeimi, E. Dehghan, D. Sanavi Khoshnoud, A. Gholizadeh, Enhancement of ferromagnetism in Ba and Er co-doped BiFeO<sub>3</sub> nanoparticles. *J. Magn. Magn. Mater.* **393**, 502 (2015)
  43. Y. Du, Z.X. Cheng, M. Shahbazi, E.W. Collings, S.X. Dou, X.L. Wang, Enhancement of ferromagnetic and dielectric properties in lanthanum doped BiFeO<sub>3</sub> by hydrothermal synthesis. *J. Alloys. Compd.* **490**, 637 (2010)
  44. M. YasinShami, M.S. Awan, M. Anis-ur-Rehman, Phase pure synthesis of BiFeO<sub>3</sub> nanopowders using diverse precursor via co-precipitation method. *J. Alloys. Compd.* **509**, 10139 (2011)
  45. X.X. Shi, X.Q. Liu, X.M. Chena, Structure evolution and piezoelectric properties across the morphotropic phase boundary of Sm-substituted BiFeO<sub>3</sub> ceramics. *J. Appl. Phys.* **119**, 064104 (2016)
  46. D. Varshney, P. Sharma, S. Satapathy, P.K. Gupta, Structural, magnetic and dielectric properties of Pr-modified BiFeO<sub>3</sub> multiferroic. *J. Alloys. Compd.* **584**, 232 (2014)
  47. S. Piskunov, A. Gopeyenko, E.A. Kotomin, YuF Zhukovskii, D.E. Ellis, Atomic and electronic structure of perfect and defective PbZrO<sub>3</sub> perovskite: Hybrid DFT calculations of cubic and orthorhombic phases. *Comput. Mater. Sci.* **41**, 195 (2007)
  48. S.A. Ivanov, R. Tellgren, F. Porcher, T. Ericsson, A. Mosunov, P. Beran, S.K. Korzhagina, P. Anil Kumar, R. Mathieu, P. Nordblad, Preparation, structural, dielectric and magnetic properties of LaFeO<sub>3</sub>-PbTiO<sub>3</sub> solid solutions. *Mater. Res. Bull.* **47**, 3253 (2012)
  49. S.V. Trukhanov, A.V. Trukhanov, V.A. Turchenko, V. Trukhanov An, D.I. Tishkevich, E.L. Trukhanova, T.I. Zubar, D.V. Karpinsky, V.G. Kostishyn, L.V. Panina, D.A. Vinnik, S.A. Gudkova, E.A. Trofimov, P. Thakur, A. Thakur, Y. Yang, Magnetic and dipole moments in indium doped barium hexaferrites. *J. Magn. Magn. Mater.* **457**, 83 (2018)
  50. V.A. Turchenko, S.V. Trukhanov, A.M. Balagurov, V.G. Kostishyn, A.V. Trukhanov, L.V. Panina, E.L. Trukhanova, Features of crystal structure and dual ferroic properties of BaFe<sub>12-x</sub>Me<sub>x</sub>O<sub>19</sub> (Me = In<sup>3+</sup> and Ga<sup>3+</sup>; x = 0.1–1.2). *J. Magn. Magn. Mater.* **464**, 139 (2018)
  51. N. Shamgani, N. Gholizadeh, Structural, magnetic and elastic properties of Mn<sub>0.3-x</sub>Mg<sub>x</sub>Cu<sub>0.2</sub>Zn<sub>0.5</sub>Fe<sub>3</sub>O<sub>4</sub> nanoparticles. *Ceram. Int.* **45**, 239 (2019)
  52. G.L. Yuan, Wing Or Siu, J.M. Liu, Z.G. Liu, Structural transformation and ferroelectromagnetic behavior in singlephase Bi<sub>1-x</sub>Nd<sub>x</sub>FeO<sub>3</sub> multiferroic ceramics. *Appl. Phys. Lett.* **89**, 052905 (2006)
  53. Y.J. Wu, X.K. Chen, J. Zhang, X.-J. Chen, Structural transition and enhanced magnetization in Bi<sub>1-x</sub>Y<sub>x</sub>FeO<sub>3</sub>. *J. Magn. Magn. Mater.* **324**, 1348 (2012)
  54. N.V. Minh, N.G. Quan, Structural, optical and electromagnetic properties of Bi<sub>1-x</sub>Ho<sub>x</sub>FeO<sub>3</sub> multiferroic materials. *J. Alloys. Compd.* **509**, 2663 (2011)
  55. M. Rahimkhani, D. Sanavi Khoshnoud, D.H. Ehsani, Origin of enhanced multiferroic properties in Bi<sub>0.85-x</sub>La<sub>0.15</sub>Ho<sub>x</sub>FeO<sub>3</sub> nanopowders. *J. Magn. Magn. Mater.* **449**, 538 (2018)
  56. P. Kubelka, New contributions to the optics of intensely light-scattering materials. Part I. *J. Opt. Soc. Am.* **38**, 448 (1948)
  57. R. Dhanalakshmi, M. Muneeswaran, K. Shalini, N.V. Giridharan, Enhanced photocatalytic activity of La-substituted BiFeO<sub>3</sub> nanostructures on the degradation of phenol red. *Mater. Lett.* **165**, 205 (2016)
  58. P.R. Vanga, R.V. Mangalaraja, M. Ashok, Effect of co-doping on the optical, magnetic and photocatalytic properties of the Gd modified BiFeO<sub>3</sub>. *J. Mater. Sci. Mater. Electron.* **27**, 5699 (2016)
  59. I.K. Konstantinou, T.A. Albanis, TiO<sub>2</sub>-assisted photocatalytic degradation of azo dyes in aqueous solution: kinetic and mechanistic investigations: a review. *Appl. Catal. B Environ.* **49**, 1 (2004)
  60. K. Wu, Y. Xie, J. Zhao, H. Hidaka, Photo-fenton degradation of a dye under visible light irradiation. *J. Mol. Catal. A Chem.* **144**, 77 (1999)
  61. H. Fu, C. Pan, W. Yao, Y. Zhu, Visible-light-induced degradation of rhodamine B by nanosized Bi<sub>2</sub>WO<sub>6</sub>. *J. Phys. Chem. B* **109**, 22432 (2005)
  62. C. Hao, F. Wen, J. Xiang, H. Hou, W. Lv, Y. Lv, W. Hu, Z. Liu, Photocatalytic performances of BiFeO<sub>3</sub> particles with the average size in nanometer, submicrometer, and micrometer. *Mater. Res. Bull.* **50**, 369 (2014)
  63. T. Gao, Z. Chena, F. Niu, D. Zhou, Q. Huang, Y. Zhua, L. Qin, X. Sun, Y. Huang, Shape-controlled preparation of bismuth ferrite by hydrothermal method and their visible-light degradation properties. *J. Alloys. Compd.* **648**, 564 (2015)
  64. T. Soltani, M.H. Entezari, Photolysis and photocatalysis of methylene blue by ferrite bismuth nanoparticles under sunlight irradiation. *J. Mol. Catal. A Chem.* **377**, 197 (2013)

**Publisher's Note** Springer Nature remains neutral with regard to jurisdictional claims in published maps and institutional affiliations.